Applied Thermal Engineering 265 (2025) 125611

Contents lists available at ScienceDirect

Applied Thermal Engineering

journal homepage: www.elsevier.com/locate/apthermeng

Research Paper

# Thermal-Hydraulic characterization in Manifold-microchannel heat sinks for Energy-efficient cooling of HEV/EV power modules

Yunseo Kim [a,1], Daeyoung Kong [b,1], R.Deepak Selvakumar [c], Minsoo Kang [d], Nana Kang [d], Jiseok Kwon [e,*], Hyoungsoon Lee [a,d,**]

[a] School of Mechanical Engineering, Chung-Ang University, Seoul 06974 South Korea
[b] Department of Mechanical Engineering, Stanford University, Stanford, CA 94305, USA
[c] Department of Mechanical and Nuclear Engineering, Khalifa University of Science and Technology, Abu Dhabi 150001, United Arab Emirates
[d] Department of Intelligent Energy and Industry, Chung-Ang University, Seoul 06974, South Korea
[e] School of Information, Communications and Electronic Engineering, The Catholic University of Korea, Bucheon-si, Gyeonggi-do, 14662, South Korea

ARTICLE INFO

*Keywords:*
Manifold microchannel
EV thermal management

ABSTRACT

Electric vehicles (EVs) require efficient cooling solutions for power modules to ensure optimal performance, reliability, and driving range. In this study, we present a comprehensive thermohydraulic analysis of manifold microchannel (MMC) heat sinks to address the unique thermal demands of EV power module cooling. We conducted a numerical analysis of the MMC geometry to evaluate its geometric variations, including manifold height (6–12 mm), inlet-to-outlet manifold width ratios (1:3–3:1), and microchannel height (1–3 mm). Their effects on pressure drop and thermal resistance were evaluated by analyzing non-uniform flow characteristics, such as flow distribution, streamwise velocity, and vorticity. This study highlights the importance of mitigating non-uniform flow effects in large-scale coolers to effectively manage the localized hotspots in EV power modules. The optimized MMC heat sink design reduced the thermal resistance and pumping power by 2.8 % and 27.3 %, respectively, when compared to traditional microchannel heat sinks (TMC). Thus, it presents an effective solution for enhancing the energy efficiency and thermal performance in EV power modules.

## 1. Introduction

Power electronics play a vital role in electric vehicles (EVs) by sustaining essential functions, such as motor control, battery management, power conversion, and regenerative braking [1].

Wide-band-gap (WBG) devices significantly enhance the EV performance owing to their higher breakdown voltages and faster switching speeds when compared to silicon-based devices, enabling equivalent power handling with smaller die sizes [2,3]. However, reducing the die size significantly increases the thermal resistance, potentially causing overheating, performance degradation, and long-term reliability issues [3]. The cooling performance can be enhanced by strongly pumping the coolant liquid. However, since nearly 30 % of the battery energy in an EV is dedicated to the thermal management of the interior and other components, this can significantly reduce the overall efficiency and adversely affect the driving range [4–6]. Therefore, numerous studies have focused on the development of coolers with reduced thermal resistance and pumping power to enhance the convective heat transfer in EV power modules [8–13].

Harpole and Eninger [14] introduced a manifold microchannel (MMC) design that incorporates larger secondary channels called and is positioned vertically over the traditional microchannels(TMC), as shown in Fig. 1(a). This design significantly reduces the pressure drop owing to the shorter effective flow paths in the microchannels. Additionally, the three-dimensional (3D) fluid path in the MMCs reduces the wall temperature via the jet impingement effect.

Table 1 summarizes the previous studies conducted on MMC heat sinks. Various experimental studies have demonstrated the outstanding thermohydraulic performance of MMC heat sinks [15–22]. Erp et al. [16] achieved outstanding performance, realizing a total thermal resistance of 0.03 W/cm$^2$ at a pressure of 51.0 kPa and flow rate of

* Corresponding author.
** Corresponding author at: School of Mechanical Engineering, Chung-Ang University, Seoul 06974, South Korea.
*E-mail addresses:* jskwon@catholic.ac.kr (J. Kwon), leeh@cau.ac.kr (H. Lee).
*URL*: http://atsla.cau.ac.kr (H. Lee).
[1] Contributed equally to this work.

https://doi.org/10.1016/j.applthermaleng.2025.125611
Received 15 September 2024; Received in revised form 11 December 2024; Accepted 15 January 2025
Available online 16 January 2025
1359-4311/© 2025 Elsevier Ltd. All rights are reserved, including those for text and data mining, AI training, and similar technologies.

**Nomenclature**

| | |
|---|---|
| $A$ | Area |
| $C_p$ | specific heat |
| $H$ | Height |
| $K$ | thermal conductivity |
| $L$ | Length |
| $\dot{m}$ | mass flow rate |
| $\Delta P$ | pressure drop |
| $q''$ | heat flux |
| $R$ | thermal resistance |
| $T$ | Temperature |
| $T$ | Thickness |
| $W$ | Width |
| $Q$ | *Volumetric flow rate* |

*Greek symbols*

| | |
|---|---|
| $M$ | dynamic viscosity |
| $P$ | Density |
| $\Gamma$ | ratio of manifold width |

*Subscripts*

| | |
|---|---|
| *Avg* | Average |
| *B* | Base |
| *Ch* | Microchannel |
| *In* | Inlet |
| *Io* | inlet manifold to outlet manifold |
| *M* | manifold |
| Max | maximum |
| Min | minimum |
| *Out* | outlet |
| *Tot* | total |
| *Wet* | wetted |
| *Heat* | Heated |

0.1–0.2 L per minute (LPM) in an Si-embedded MMC. Kong et al. [18] addressed the fabrication complexity of MMCs using the laser powder bed fusion process along with 3D printing and achieved a thermal resistance of 0.15 W/cm$^2$ at a pressure drop of 1.71 kPa under a flow rate of 0.1–0.4 LPM. To understand and enhance the complex flow characteristics of the MMC, geometrical analyses were conducted based on numerical modeling [22–28]. Extensive research has been conducted on developing novel geometries and optimizing parameters to improve the thermohydraulic performance of MMC heat sinks. However, the cooling of localized heat sources with MMC heat sinks remains a major challenge, since most studies involve simplifying the cooler domain to a unit cell with a constant heat flux at the base for cost efficiency, as shown in Fig. 1(b). This is because the thermal hydraulic efficiency significantly varies based on the non-uniformities in the flow and convection across the system, as shown in Fig. 1(c). Particularly in EV power module cooling, where the direct bonded copper (DBC) area (cooler area) is 50 times larger than the chip, localized weakening of convection around the chip area can cause a significant temperature increase. Conversely, an uneven flow that is adjusted to provide intensive cooling to the chips can enhance the thermohydraulic efficiency. Therefore, it is crucial to understand the impact of geometric variables on the local thermohydraulic properties for developing cooling solutions to mitigate the hot spots in EV power modules [29].

To this end, a full-scale simulation on the SiC power module was conducted to evaluate the effects of geometric design variables, including manifold height-to-width ratios and microchannel height. The thermohydraulic performance was analyzed with a particular focus on the local flow characteristics, grounded in fluid distribution, vorticity, and local velocity profiles.. Since most existing studies have been conducted at significantly lower flow rates, typically under 1 LPM, this study was conducted at a typical EV cooling system flow rate of around 10 LPM to identify potential deviations under varying flow conditions [30].

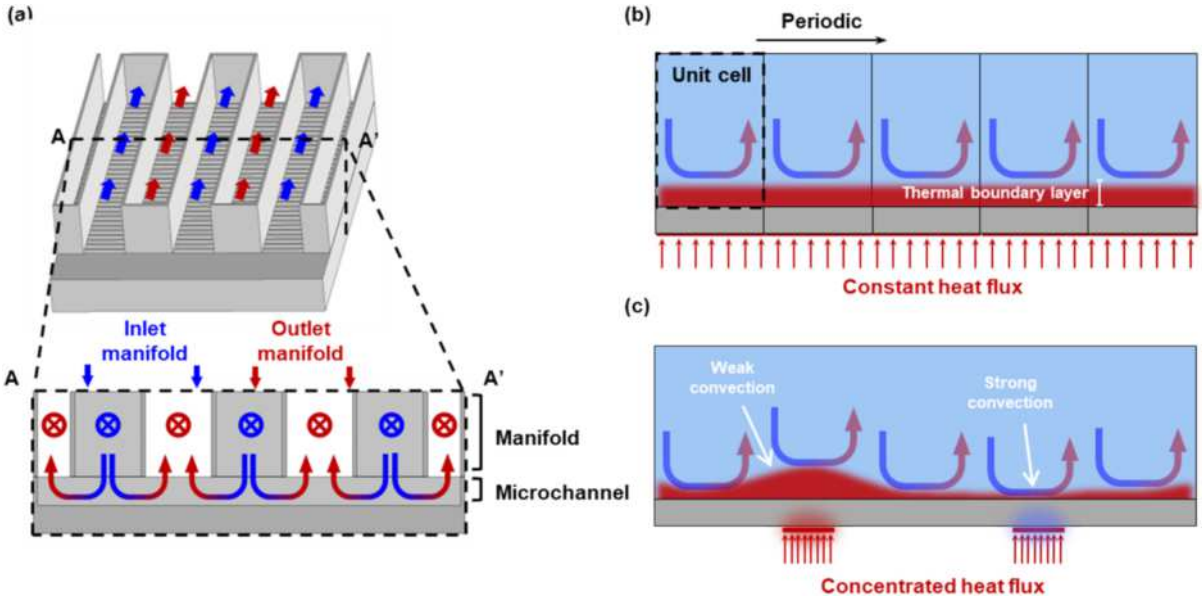


**Fig. 1. Schematic illustration of (a) the flow path in an MMC heat sink, (b) the periodically implemented unit cell approach, and (c) the actual non-uniform thermal boundary through the MMC.** The working fluid is vertically distributed in the inlet manifold of microchannel and exits from the outlet manifold.

## 2. Methods

### 2.1. Computational domain and geometrical and operational variables of the MMC heat sink

Fig. 2(a) presents a schematic of a conventional 2-in-1 SiC power module, where the heat generated at the power device junction is conducted through the attached layers and DBC before being dissipated into the coolant via the heat sink [31]. To reduce the computational costs and focus on the convective heat transfer, the packaging interfaces with conductive layers were simplified by using the surface areas of chips 1 and 2 that functioned as heat sources, as shown in Fig. 2(b).

Fig. 3(a) depicts the computational domain of the MMC heat sinks, reflecting the design of a commercial EV SiC power module with two chips. The overall dimensions of heat sinks are 41.5 mm × 30.6 mm × (22.0–29.0) mm ($x \times y \times z$) with a footprint area of 635.0 mm$^2$, aligned with the DBC layer and wetted area. The 2-mm-thickness base of the MMC heat sink ($t_b$) contained 32 microchannels with the wall thickness ($t_{ch}$) and width ($W_{ch}$) of 0.3 and 0.8 mm, respectively. The manifold wall ($t_m$) thickness was set to 0.3 mm. To reduce computational resources, a symmetrical half-section along the *x-z* plane was utilized, as indicated by the green dashed lines.

We primarily explored the impact of various geometric variables on the flow morphology and distribution within an MMC heat sink that affects its overall thermal and hydraulic performance. To achieve this, the following three key parameters were adjusted: (i) manifold height ($H_m$), (ii) ratio of the inlet-to-outlet manifold widths $\Gamma_{io}$ ($W_{in}$: $W_{out}$), and (iii) microchannel height ($H_{ch}$); each parameter was varied across different levels, as graphically presented in Fig. 3(b–d).To optimize the design of EV power modules, we assessed the flow rates within 0.5–8 LPM. These values span from lower levels referenced in the MMC literature to higher levels prevalent in EV cooling systems. Table 2 details each parameter setup.

### 2.2. Governing equations and boundary conditions

By employing a conjugate heat transfer computational model, the thermohydraulic performances of various MMC heat sinks were investigated using the ANSYS Fluent software. The model featured a 3D, single-phase, steady, and incompressible fluid flow with the exclusion of heat loss from radiation, viscous dissipation, and gravitational force. A standard SST k-omega turbulent model was implemented to account for the turbulent flows owing to complex high-flow-rate conditions [32]. Supplementary Note 1 presents the detailed expressions of the governing equations.

The following boundary conditions were considered at appropriate locations within the computational domain to numerically solve the governing equations. The working fluid entered the inlet manifold at a constant flow rate with $T_{in} = 293.15$ K. A constant and uniform heat flux of 500 W/cm$^2$ was dissipated using two distinct chips, each measuring 25 mm$^2$ and spaced 9.1 mm apart. Natural convection on the top surface of the MMC was accounted for using a convection heat transfer coefficient of 10 W/m$^2$K and free stream temperature of 378.15 K. An ambient pressure outlet boundary condition was applied at the manifold outlet, and a no-slip boundary condition was enforced at the fluid–solid interface. To minimize computational costs, a half-size model of the MMC was used, incorporating a symmetric boundary condition along the central plane at $y = 15.3$ mm. The manifold and microchannel were constructed from Al1060, and a water–ethylene glycol mixture with a 50 % weight ratio served as the working fluid. The thermophysical properties of the fluid varied with temperature, whereas its solid properties remained constant. Temperature gradients significantly influence turbulent heat transport but have negligible effects on solid conduction [33]. Table 3 lists all thermophysical properties.

### 2.3. Numerical procedure and grid sensitivity analysis

The governing equations were discretized using a control-volume-based finite-difference method on a non-uniform structured grid with hexahedral cells. The convection and diffusion terms in the governing equations were discretized using the second-order upwind and central-differencing schemes, respectively. The SIMPLE algorithm was utilized for pressure–velocity coupling. The iterative solution converged when the residuals of the velocity and energy equations were less $1 \times 10^{-6}$ and $1 \times 10^{-9}$, respectively. The computational grid was selected based on a grid sensitivity analysis, the results of which are detailed in Fig. S1. Four grids with cell counts ranging from 3.3 million to 32 million were evaluated. The variations in pressure drop and average heater surface temperature became negligible when the grid resolution exceeded 14 million cells; therefore, grids with cell counts ranging from 14 million to 16 million were employed.

## 3. Results and discussion

This section presents the numerical investigation results of the thermohydraulic characteristics of full-scale MMC heat sinks. This examination covered ten cases (A–J) that featured diverse combinations of geometric parameters at various flow rates.

### 3.1. Flow morphology in the MMC heat sink

The turbulence generated by the unique 3D flow path within the

**Table 1**
Summary of literature on MMC heat sink.

| Work | Authors | Geometrical variation | | $Q_{total}$ [LPM] | $A_{heat}$ [mm$^2$] | $A_{wet}$ [mm$^2$] | $R_{total}$ [cm$^2$K/W] | ΔP [kPa] |
|---|---|---|---|---|---|---|---|---|
| | | Manifold | Microchannel | | | | | |
| Experimental | Jung et al.2019[15] | – | – | 0.03—0.10 | 5 × 5 | 5 × 5 | 0.15 | 2.60 |
| Experimental | Erp et al.2020[16] | $t_m$ | – | 0.0048—0.048 | 3 × 3 | 6 × 6 | 0.03 | 51.00 |
| Experimental | Yang et al.2022[17] | – | $t_{ch}$, $W_{ch}$ | 0.31—0.61 | 20 × 20 | 20 × 20 | 0.21 | 35.00 |
| Experimental | Kong et al.2023[18] | – | – | 0.10—0.40 | 10 × 10 | 10 × 10 | 0.15 | 1.71 |
| Experimental | Kim et al.2023 [19] | – | – | 0.02—0.05 | 5 × 5 | 5 × 5.5 | 0.29 | 0.59 |
| Experimental | Kong et al.2024[20] | – | $W_{ch}$ | 0.03—0.19 | 5 × 5 | 5 × 5 | 0.10 | 24.70 |
| Experimental | Yang et al.2024[21] | Overall type | $t_{ch}$, $W_{ch}$, $H_{ch}$ | 0.12—0.36 | 20 × 20 | 20 × 20 | 0.08 | 54.50 |
| Unit cell | Ryu et al.2003[22] | $\Gamma_{io}$ | $t_{ch}$, $H_{ch}$ | – | – | – | – | – |
| Unit cell | Sarangi et al.2014[23] | $\Gamma_{io}$ | – | – | – | – | – | – |
| Unit cell | Pan et al.2022[24] | – | $H_{ch}$ | – | – | – | – | – |
| Unit cell | Lin et al.2021[25] | Overall type | – | – | – | – | – | – |
| Unit cell | Chen et al.2022[27] | – | Overall type | – | – | – | – | – |
| Unit cell | Yang et al.2023[28] | Overall type, $\Gamma_{io}$ | – | – | – | – | – | – |
| Full scale | This work | $H_m$, $\Gamma_{io}$ | $H_{ch}$ | 0.5—16.0 | 5 × 5 | 42 × 31 | 0.10 | 18.28 |

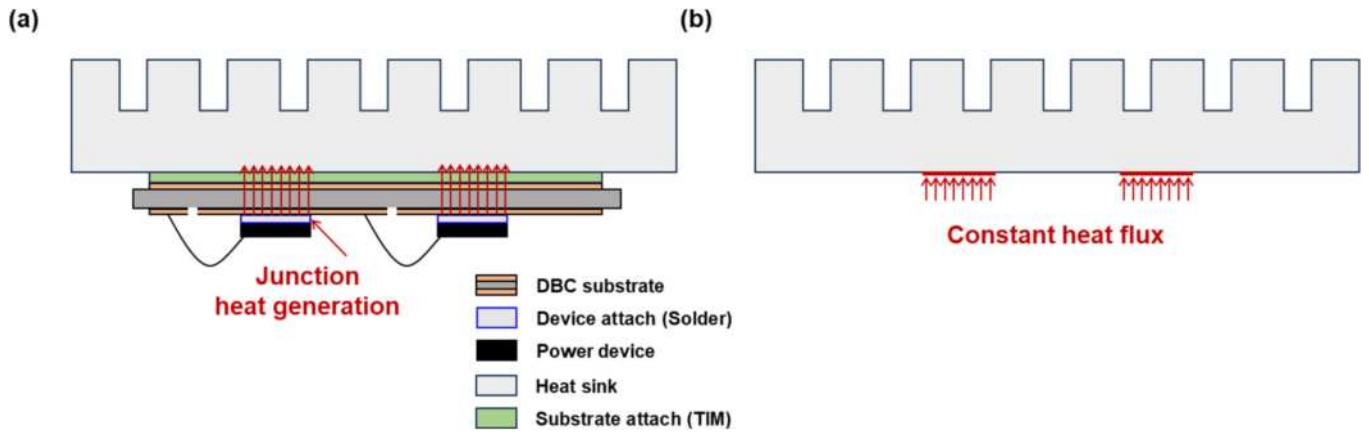


**Fig. 2. Schematic illustration of** conventional 2-in-1 SiC power module cooling architecture packaging layers with heat generation at the device junction, and (b) a simplified model with constant heat flux conditions.

MMC heat sink significantly affects the pressure drops and fluid distribution, as will be elucidated in the subsequent sections. To this end, Fig. 4(a–c) illustrates the flow morphology within the MMC heat sink is illustrated using streamlines, velocity profiles, and pressure contours for Case A at a flow rate of 8 LPM. The pressure drops in the internal flow are typically classified into major and minor losses. The major losses refer to frictional losses that occur along the straight sections of the flow path, while the minor losses are attributed to turbulent dissipation caused by flow disruptions due to geometric elements. While TMCs primarily comprise straight flow paths, MMCs feature intricate flow paths and pressure gradients that induce minor losses.

Fig. 4(a) shows an abrupt flow contraction transitioning from the inlet plenum to the manifold, forming vena contracta around the front section of the inlet manifold (indicated by black dashed lines). This high-velocity region is surrounded by small recirculating flow cells, and the rear section exhibits a large stagnation zone (indicated by white dashed lines). A circulating flow is formed when the fluid orients toward the microchannels after colliding with the rear wall of the inlet manifold. These two distinct local flow phenomena significantly affect the static pressure distribution, as shown in Fig. 4(c). Low pressure is observed around the vena contracta owing to the energy loss within the recirculating zone. Conversely, in the stagnation zone, the static pressure increases owing to the conversion of kinetic energy to static pressure. Notably, the flow within the MMC heat sink experiences additional minor loss owing to contraction and rotation at the 1) inlet plenum/manifold and 2) manifold/microchannel junctions. However, the total pressure-drop decreases since significant the major losses within the microchannel section are reduced by routing the flow through the manifold.

### 3.2. Flow distribution of microchannels

Flow non-uniformity arises along the x-direction owing to each microchannel receiving a different amount of fluid from the manifold, causing variations in the flow rates. Understanding the underlying mechanisms of the flow maldistribution is crucial for designing MMC heat sinks with enhanced thermohydraulic performance.

Fig. 5 shows the supplied mass flow rate in each microchannel for varying (a) total flow rates, (b) manifold heights, (c) ratios of inlet to outlet manifold widths, and (d) microchannel heights. These localized flow phenomena led to a nonuniform flow distribution because the varying pressure force inside the inlet manifold unequally directed the fluid into microchannels. The MMC heat sink comprised 32 microchannels, with Channels 1–3 located near the front corresponding to lower mass flow rates despite exhibiting backflows from the microchannels. This can be attributed to the reduced pressure force around the vena contracta, as shown in Fig. 4(a). Contrastingly, the channels closer to the rear section exhibited higher flow rates owing to strong pressure force within the stagnation zone. As shown in Fig. 5(a), these effects intensify with increasing fluid velocity, leading to a more pronounced non-uniformity in the flow, particularly for cases with higher total flow rates. Fig. 5(b) shows that the flow distribution changes with varying the manifold heights in the range $H_m$ = 6–12 mm. Additionally, the flow uniformity improves owing to the reduced fluid velocity within a larger manifold cross section. The most and least sever non-uniformities in the flow distribution are observed at $H_m$ = 6 mm and $H_m$ = 12 mm, respectively. Fig. 5(c) shows the effect of $\Gamma_{io}$ on the flow uniformity within the microchannels. Contrasting trends were observed between Channels 1–3 and other channels; the flow supply in the former improved with a wider inlet manifold owing to the reduced pressure drop caused by the sudden contraction around the inlet plenum. Conversely, Channels 4–32 attained better flow uniformity with a narrow inlet manifold width, which is attributed the change in flow resistance determining the flow distribution at each possible inlet–outlet path. Fig. 6(a) and (b) represent the two distinct flow paths within the MMC; Paths 1 and 2 traverse the microchannels and flow near and around the rear section of the manifold, respectively. The modification in the width and cross-sectional area of the manifold affects the flow resistance along each path, consequently impacting the flow distributions within microchannels because more fluid passes through the least-resistant path. Particularly, an increased ratio of the inlet-to-outlet manifold width reduces and increases the flow resistance along the inlet and outlet manifolds, respectively. Consequently, more fluid favored Path 2, which had a longer distance within the inlet manifold, and was supplied to the microchannels around the rear section. Fig. 5(d) shows that a reduction in the microchannel height yields a more uniform flow distribution. By reducing the cross-sectional area within the microchannels, the overall flow resistance along each path increased equally, thereby mitigating the effects of local flow phenomena.

In Fig. 7(a–c), the streamlines are contoured by the vorticity magnitude, providing a visual representation of vortex formation within the microchannel flow. The fluid entering the microchannel from the inlet manifold changes its direction by impacting the right upper wall and experiencing parallel inertia and vertical pressure force. This 90° change in direction gives rise to an angular momentum within the fluid, thereby generating a streamwise vortex along the *y*-direction. In cases characterized by lower flow rates, as shown in Fig. 7(a) and (b), the flow within the microchannels maintain a smooth profile. The angular momentum is rapidly dissipated, forming a U-shaped path during the entry and exit of the fluid. Contrastingly, higher flow rates and consequent strong impacts induced the formation of streamwise vortices that persisted throughout the microchannel, as shown in Fig. 7(c).

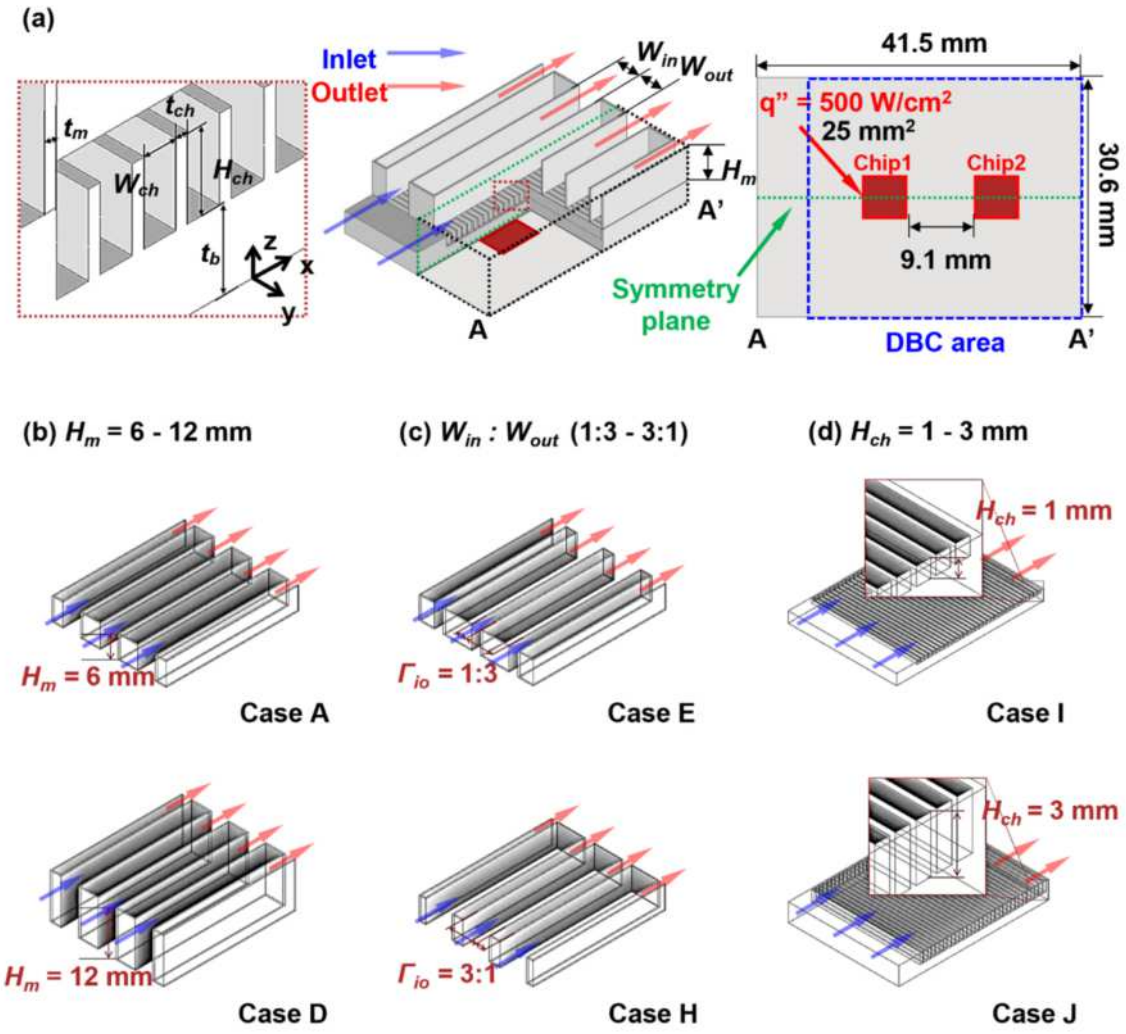


**Fig. 3. Full-Scale MMC heat sink geometry.** (a) Schematic of the computational domain depicting symmetric conditions and chip configuration. Comparison of two representative cases highlighting the largest differences for each geometric parameter: (b) manifold heights, (c) ratios of inlet-to-outlet manifold width, and (d) microchannel heights.

**Table 2**
Matrix of the considered test cases.

| | Microchannel | | | | Manifold | | |
|---|---|---|---|---|---|---|---|
| | $t_b$ | $t_{ch}$ | $W_{ch}$ | $H_{ch}$ | $t_m$ | $H_m$ | $\Gamma_{io}$ |
| **Case A** | 2 | 0.3 | 0.8 | 2 | 0.3 | 6 | 1:1 |
| **Case B** | 2 | 0.3 | 0.8 | 2 | 0.3 | 8 | 1:1 |
| **Case C** | 2 | 0.3 | 0.8 | 2 | 0.3 | 10 | 1:1 |
| **Case D** | 2 | 0.3 | 0.8 | 2 | 0.3 | 12 | 1:1 |
| **Case E** | 2 | 0.3 | 0.8 | 2 | 0.3 | 6 | 1:3 |
| **Case F** | 2 | 0.3 | 0.8 | 2 | 0.3 | 6 | 1:2 |
| **Case G** | 2 | 0.3 | 0.8 | 2 | 0.3 | 6 | 2:1 |
| **Case H** | 2 | 0.3 | 0.8 | 2 | 0.3 | 6 | 3:1 |
| **Case I** | 2 | 0.3 | 0.8 | 1 | 0.3 | 6 | 1:1 |
| **Case J** | 2 | 0.3 | 0.8 | 3 | 0.3 | 6 | 1:1 |

Units are in mm.

**Table 3**
Thermophysical properties of water–ethylene glycol and aluminum.

| | Fluid | Solid |
|---|---|---|
| | Water-ethylene glycol | Aluminum |
| $\mu$ [N·s/m$^2$] | $1.441 \times 10^{19}\, T^{-8.733}$ | – |
| $k$ [W/(m·K)] | $2.14 \times 10^{-1}\, T^2 + 1.33 \times 10^{-3}\, T$–$2.24 \times 10^{-6}$ | 234 |
| $\rho$ [kg/m$^3$] | $1.08 \times 10^{3}\, T^2 + 4.40 \times 10^{-1}\, T$–$1.70 \times 10^{-3}$ | 2705 |
| $C_p$ [J/(kg·K)] | $2.55 \times 10^{3}\, T + 3.15$ | 900 |

### 3.3. Thermohydraulic behavior inside the microchannel

To quantitatively assess the impact of geometric variables on fluid motion inside the microchannel, Fig. 8(a–c) and Fig. 9(a–c) present the

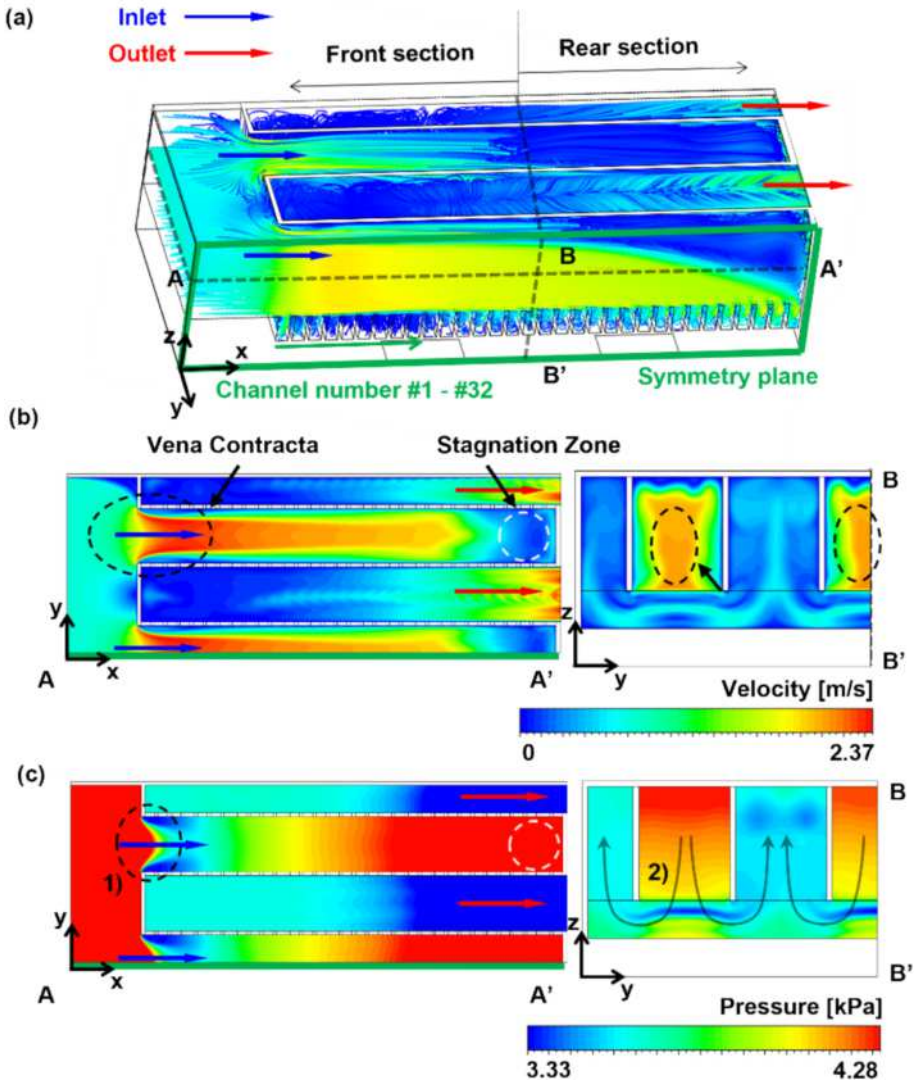


**Fig. 4. Flow morphology within the full-scale MMC heat sink** (a) Streamlines on a half-domain with contours of the velocity magnitude. (b) Velocity and (c) pressure contours at the center plane in Case A under a flow rate of 8 LPM. Distinct flow phenomena, including vena contracta and stagnation zones, are depicted. These regions influence the static pressure distribution and expose extra pressure losses in the MMC heat sink.

velocity and vorticity distributions with respect to the microchannel flow direction (*y*-direction) and referred to as the streamwise velocity and vorticity, respectively. Channels 21, 23, and 27 were selected for each geometric variable for comparison under the same mass-flow rate conditions to identify the influence of geometrical variations on fluid motion (red circles in Fig. 5).

Fig. 8(a)–(c) show the streamwise velocity distributions within a single microchannel for various values of $H_m$, $\Gamma_{io}$, and $H_{ch}$. The flow rate was fixed at 8 LPM because the streamwise vortex within the microchannel became more pronounced at relatively higher total flow rates, as shown in Fig. 7. The structural characteristics of MMC result in the following trend: As the fluid enters and exits the microchannel vertically, the streamwise velocity becomes zero at the stagnation point below the center of each inlet/outlet of the manifold, where the flow is symmetrically divided and merged on both sides. The maximum streamwise velocity occurs below the manifold wall, where the flow passes through the smallest cross-section at the highest rate. Fig. 8(a) shows the uniformity of the streamwise velocity distribution for various $H_m$ values, underscoring the influence of flow rate, over the total cross-sectional area, on the streamwise velocity. Fig. 8(b) reveals that variations in $\Gamma_{io}$ shift the peaks and troughs of streamwise velocities; however, the peak intensity remains unchanged. Fig. 8(c) shows that increasing $H_{ch}$ decreases the overall magnitude of streamwise velocity because the peak value is inversely proportional to the cross-sectional area beneath the manifold wall.

The streamwise vortex discussed in Section 3.2 considerably improves the heat transfer by suppressing the growth of the thermal boundary layers along the side walls and bottom of the microchannel. The streamwise vortex can be characterized by Y-vorticity, which measures the curl of the velocity field. Fig. 9(a–c) show the impact of varying $H_m$, $\Gamma_{io}$, and $H_{ch}$ values on streamwise vorticity within the microchannel, which is typically greater near the manifold inlet and minimum in channels close to the manifold outlet. This trend indicates the formation of a streamwise vortex near the inlet and its gradual weakening along the flow toward the manifold wall, where the angular momentum transitions into linear momentum, as shown in Fig. 7(c). Fig. 9(a) shows that decreasing the manifold height results in increased streamwise vorticity values below the inlet manifold. This can be attributed to the higher *x*-directional velocity within the manifold, which exerted a stronger impact on the microchannel wall and induced a more robust vortex. As shown in Fig. 9(b), decreasing $\Gamma_{io}$ leads to greater streamwise vorticity, further amplified by the strong impact. The

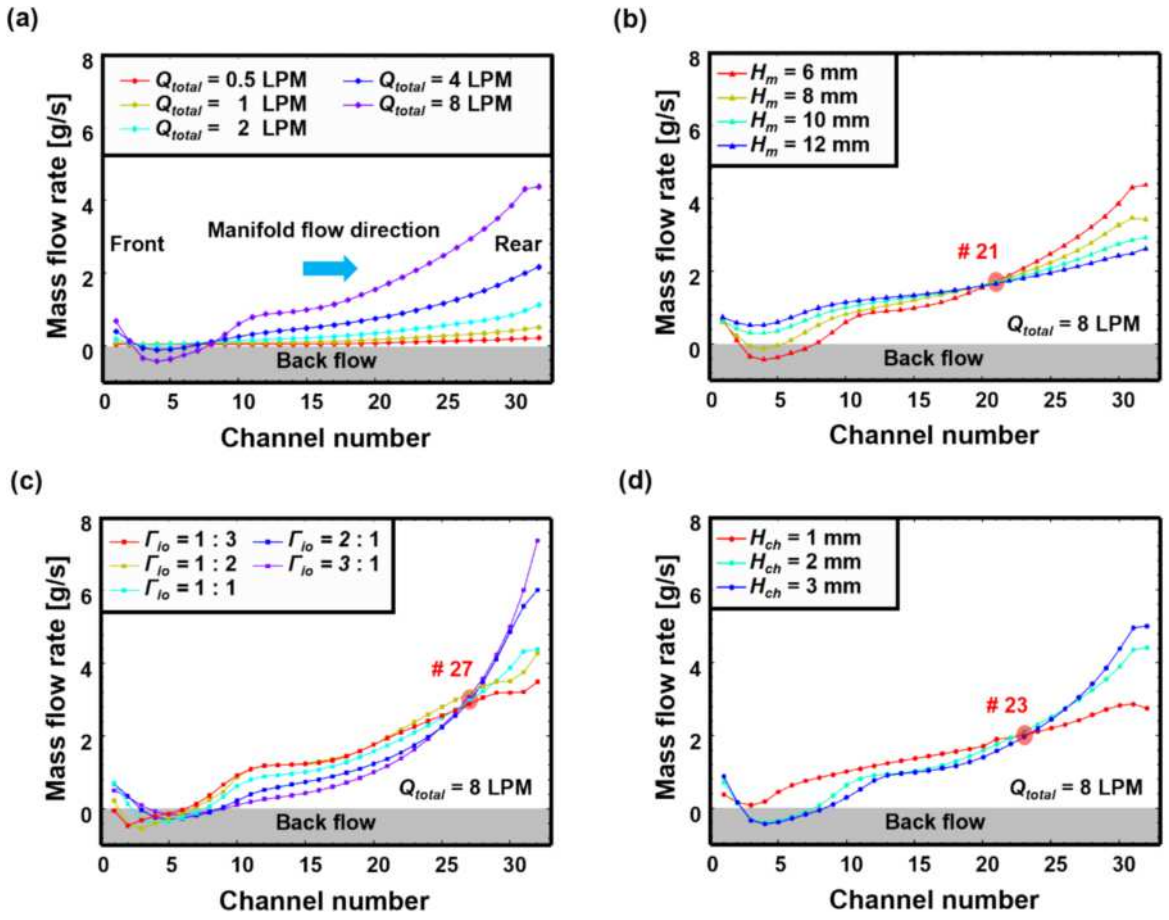


**Fig. 5. Mass flow rate across each microchannel at various parameters.** (a) Total flow rate, (b) manifold height, (c) ratio of inlet-to-outlet manifold width, and (d) microchannel height. Microchannels near the front section experience lower mass flow rates, including backflows, attributed to the reduced pressure force around the vena contracta. The channels near the rear section experience higher flow rates owing to strong pressure force within the stagnation zone.

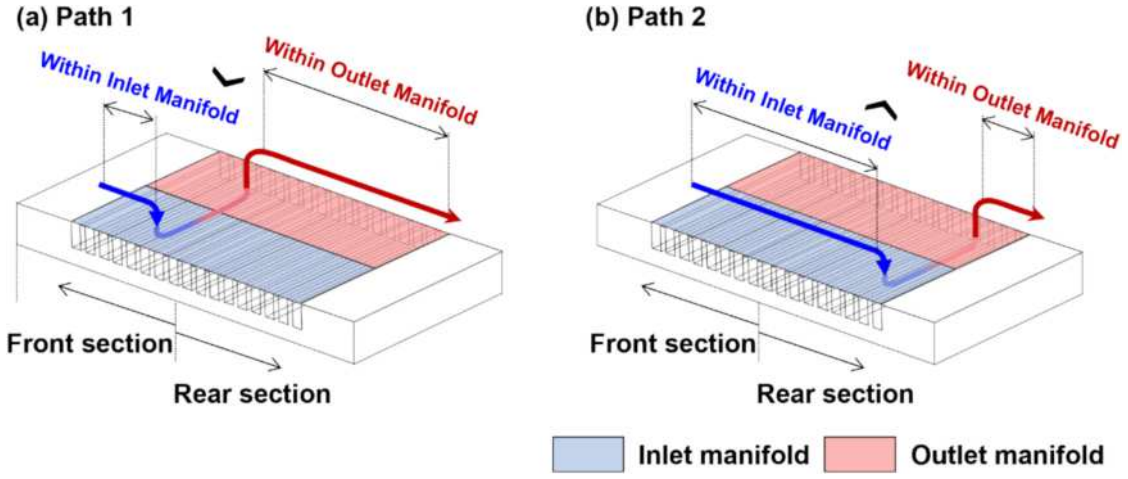


**Fig. 6. Schematic of the two flow paths within the MMC heat sink.** (a) Path 1 through channels near the front section and (b) Path 2 through channels near the rear section. Paths 1 and 2 have a longer distance of travel within the outlet and inlet manifolds, respectively.

narrowest inlet manifold width (indicated in red) causes a sharp decline in the streamwise vortex after it traverses the manifold wall, resulting in lower values below the outlet manifold compared with the curve representing the widest inlet (in violet). Fig. 9(c) shows that the streamwise vorticity increases with a decreasing microchannel height because the rotating motion accelerates with a smaller turning radius.

Fig. 10(a–c) show the heat transfer coefficient (HTC) distributions within the microchannels with geometrical variations. HTC is defined as the local heat flux divided by the difference between the wall and inlet fluid temperatures. The flow characteristics shown in Fig. 8 and Fig. 9 correspond to the heat transfer characteristics. Particularly, a high velocity replenishes the cold liquid, and the vortex cools the heated wall via mixing action. Among the vortices with three orientations (rotating axes of $x$ ,$y$, and $z$), the streamwise vortex (in the $y$-direction) was the

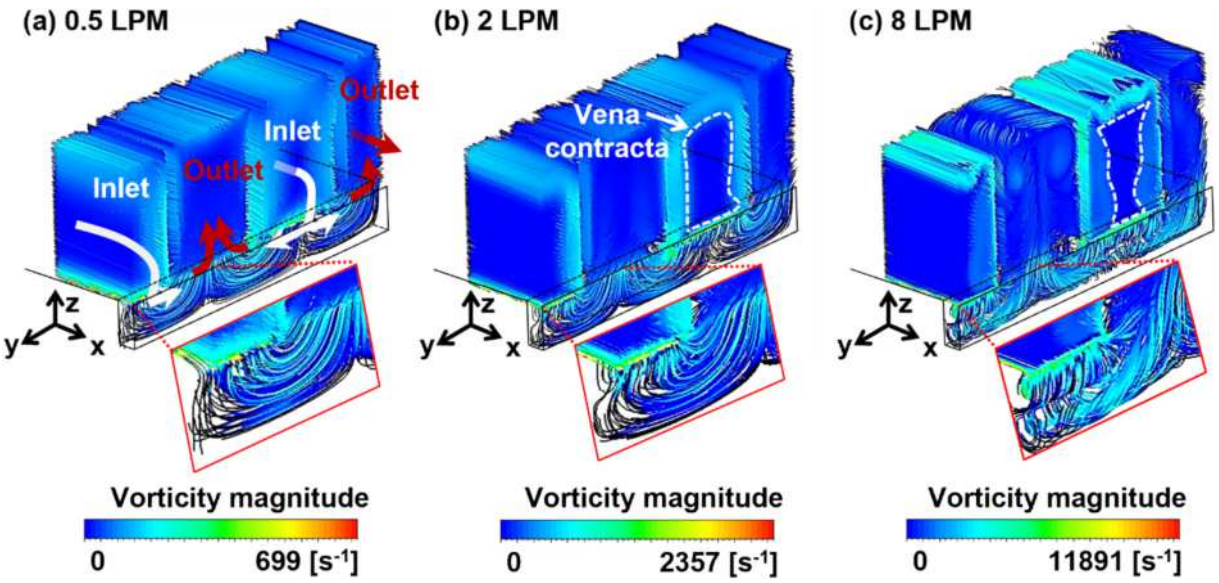


**Fig. 7. Streamlines at the center of the MMC heat sink with vorticity magnitude contours.** Vortex formation in the microchannel flow is depicted at the following flow rates: (a) 0.5 LPM, (b) 2 LPM, and (c) 8 LPM. Lower flow rates exhibit a smooth profile, whereas higher flow rates induce persistent streamwise vortex along the microchannel.

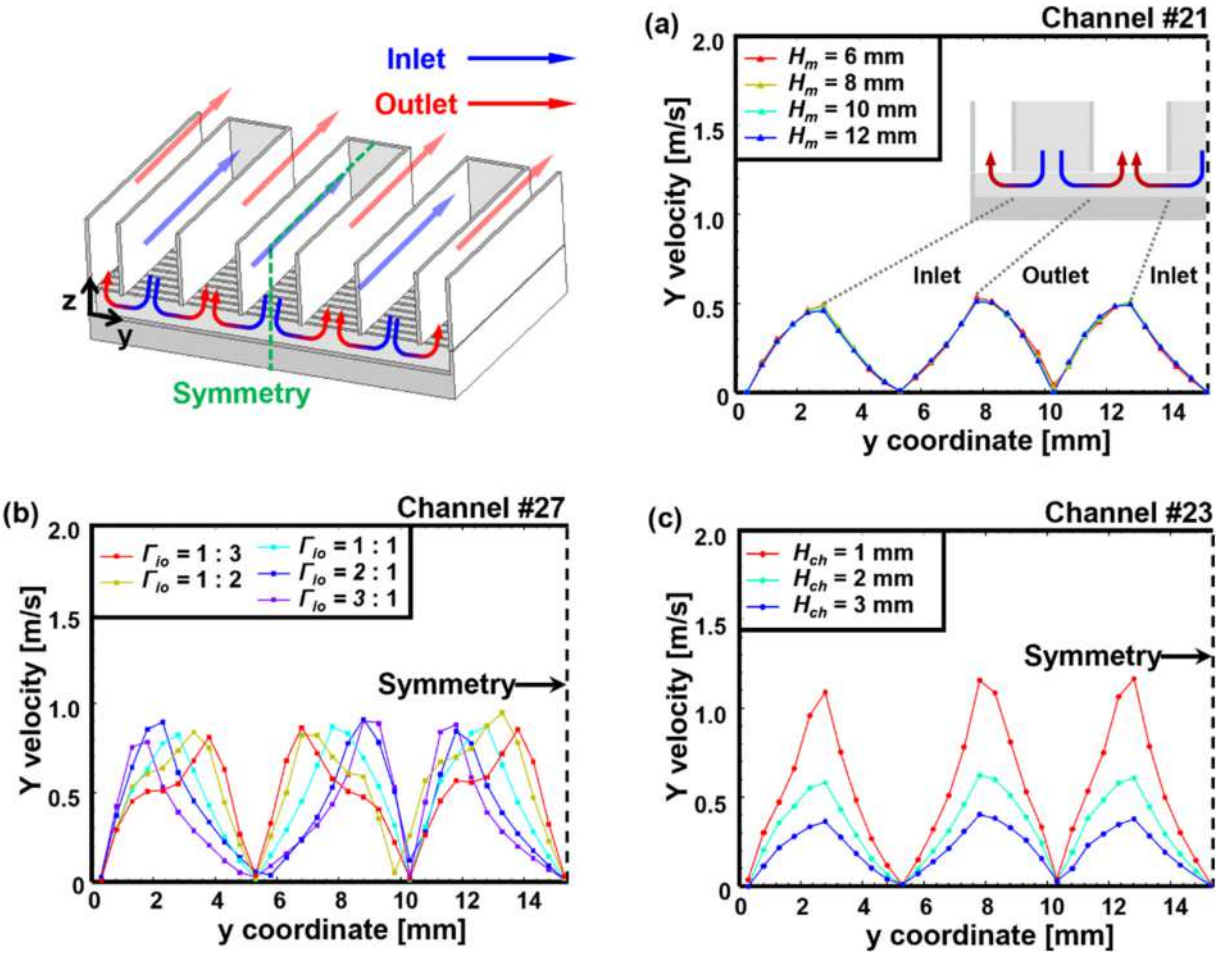


**Fig. 8. Comparison of the streamwise (*y*-direction) velocity distribution within a single microchannel.** Total flow rate is fixed at 8 LPM and variations in (a) manifold height, (b) ratio of inlet-to-outlet manifold width, and (c) microchannel height are explored. Stagnation points appear below the manifold center with zero velocity, and streamwise velocity peaks beneath the manifold wall.

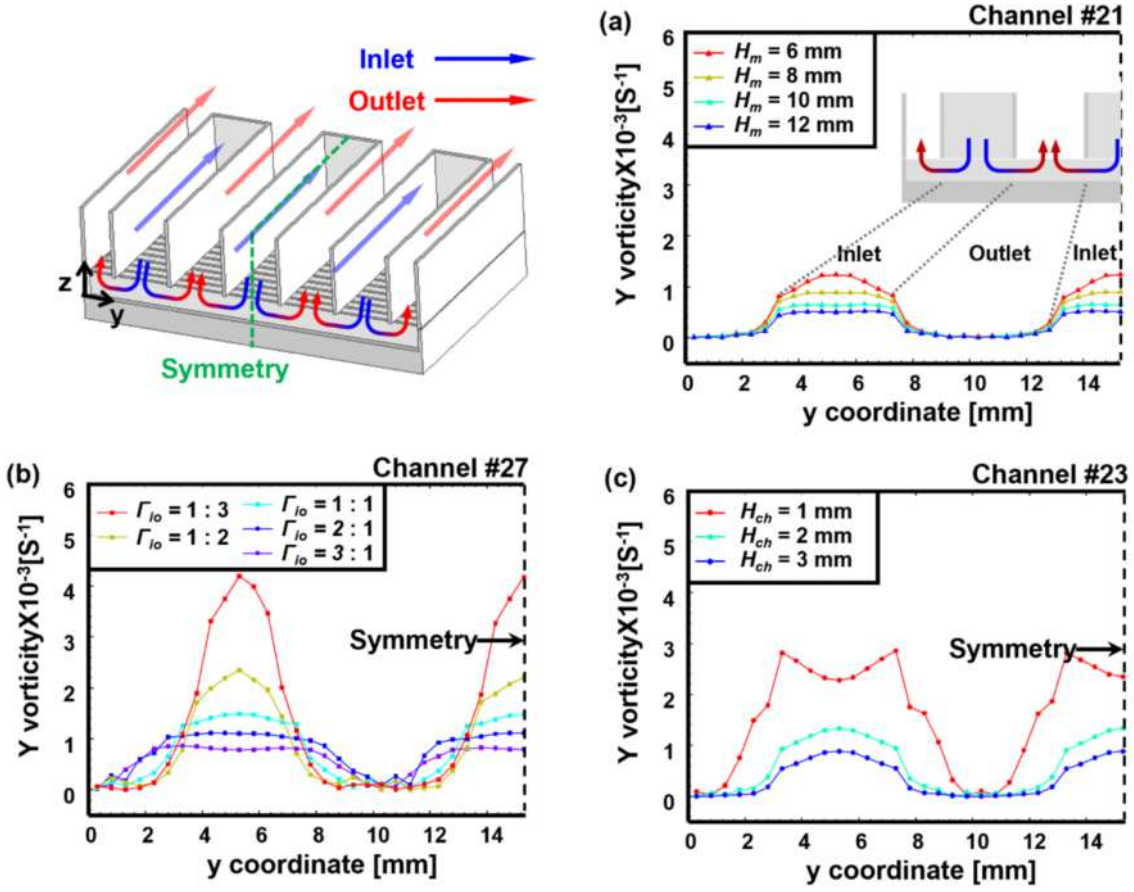


**Fig. 9. Comparison of the streamwise (y-direction) vorticity distribution within a single microchannel.** Total flow rate is fixed at 8 LPM and streamwise vorticity distributions are compared by varying (a) manifold height, (b) ratio of inlet-to-outlet manifold width, and (c) microchannel height. Streamwise vortex, which appears below the inlet manifold and disappears beneath the outlet manifold, intensifies with decreasing inlet manifold width and microchannel height.

most effective at penetrating the thermal boundary layer on the wall, thereby enhancing heat transfer. Consequently, Fig. 10(a–c) show that the HTC distribution is analogous to the profile shapes of streamwise vorticity and velocity. Hence, the uneven flow characteristics within the microchannel significantly influence the local heat transfer distributions. Particularly, the combined effects of flow stagnation, inertia, and vortex action at each location determine the local heat transfer distribution. Higher and lower HTC values were observed in the regions below the inlet manifold and around the outlet manifold, respectively, reflecting the patterns observed in the streamwise vorticity distribution. Despite the occurrence of maximum vorticity below the center of each manifold, the peak HTC shifted away from the center owing to the lack of replenishment caused by flow stagnation. Consequently, if the manifold height decreases or the width of the inlet manifold narrows, the HTC distribution beneath the inlet manifold improves owing to the enhanced streamwise vortex (Fig. 10(a–b)). Additionally, a decrease in the channel height, increases the velocity, vorticity, and HTC across the entire microchannel wall (Fig. 10(c)).

### 3.4. Non-uniform temperature distribution in the MMC heat sink

Fig. 11 shows the (a),(b) temperature contours and (c),(d) velocity contours at the center plane of the inlet manifold. A comparison between two different flow rates of (a),(c) 0.5 LPM and (b),(d) 8 LPM shows that the high total flow rate condition in the EV power module poses a risk of drastic temperature rise owing to severe flow maldistribution. Chip 1, which is cooled by the fluid flowing through the front microchannels, exhibited a higher temperature compared to Chip 2, which is cooled by the rear microchannels. The discrepancy in the temperature between the two chips is attributed to the uneven flow distribution across the microchannels, as shown in Fig. 11(c),(d).Compared to the rear microchannels, the front microchannels exhibit a thicker thermal boundary layer owing to the reduced flow at a flow rate of 0.5 LPM. The non-uniformity in flow supply and its impact on the heat transfer imbalance become more pronounced with increasing total flow rate. At 8 LPM, the rear microchannels exhibit a thin thermal boundary layer owing to abundant fluid supply and momentum. Conversely, the front microchannels experience hindered convection with flow stagnation, causing a significant temperature increase in the fluid and Chip 1.

### 3.5. Thermohydraulic performance evaluation

The thermal–hydraulic performances of various MMC heat sinks were quantified in terms of total thermal resistance and pressure drop. Three distinct geometrical variations, including different manifold heights (Cases A–D), ratios of inlet-to-outlet manifold widths (Cases A, H), and microchannel heights (Cases A, I, and J), were compared across the total flow rates of 0.5, 4, and 8 LPM. The total thermal resistance is defined as the difference between the maximum chip and inlet fluid temperatures divided by the applied heat flux. The pressure drop is

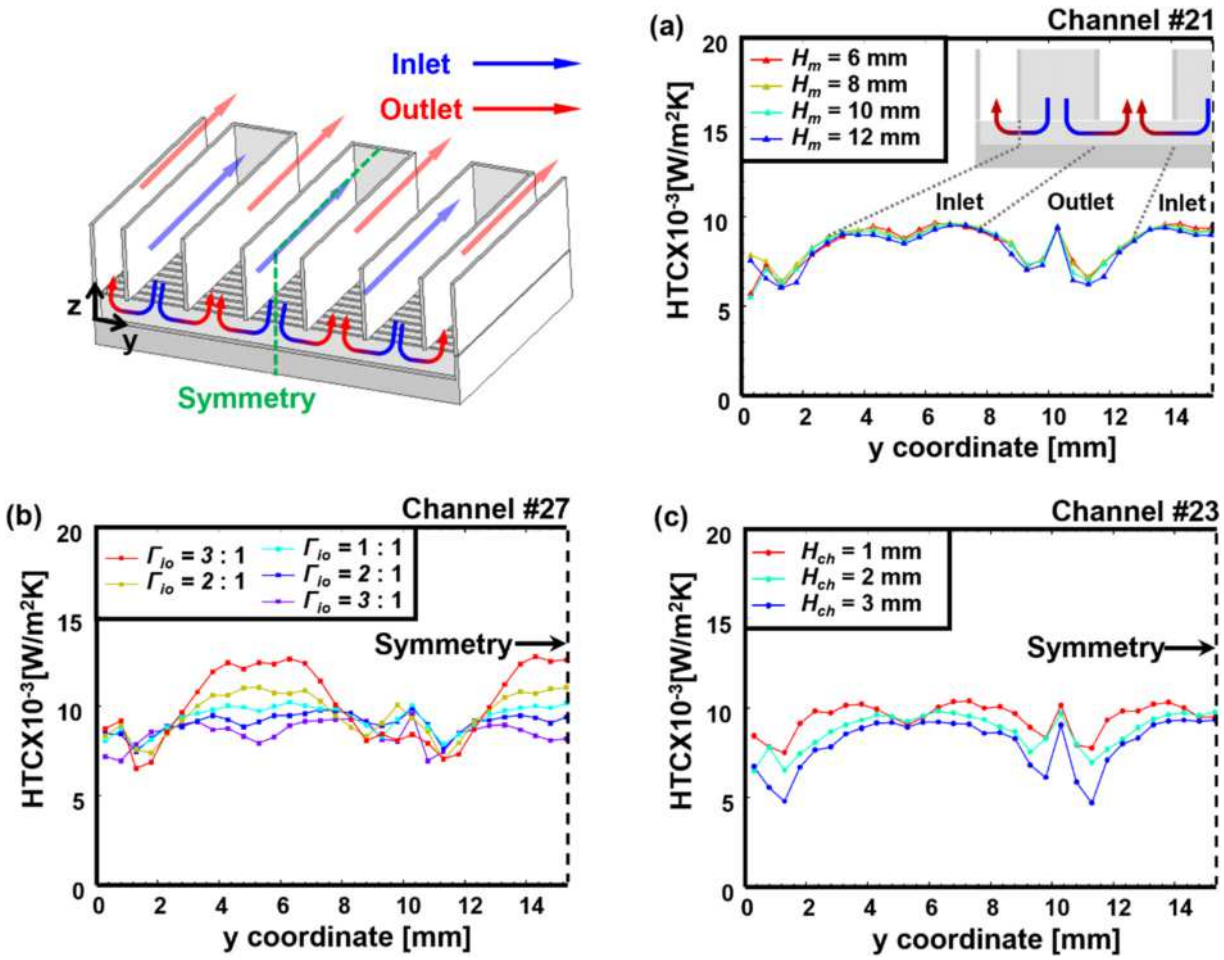


**Fig. 10. Heat transfer coefficient distribution within a single microchannel at a total flow rate of 8 LPM.** Variations in heat transfer coefficient are compared with (a) manifold height, (b) ratio of inlet-to-outlet manifold width, and (c) microchannel height. A strong relation between streamwise vorticity and velocity is observed, indicating the combined effect of flow stagnation, inertia, and vortex on enhancing the heat transfer.

calculated as the area-weighted average of the fluid at the inlet and outlet of the MMC heat sink.

As shown in Fig. 12(a), the total thermal resistance decreases slight with increasing manifold height at all flow rates. Fig. 9 shows a stronger mixing effect at lower manifold heights; however, this effect was only observed for the rear microchannels. The severe lack of flow around the front microchannels led to a significant increase in the maximum temperature of Chip 1. Fig. 12(b) indicates that increasing the manifold height results in an improved pressure drop. A low fluid velocity in manifolds with increased height reduces the pressure loss that occurs during flow contraction at each junction. Increasing the manifold height contributes to the most significant reduction in pressure losses. This enables higher flow rates at the same pumping power, indicating potential enhancements in the thermal performance. Our results demonstrate that the flow maldistribution over a large footprint area establishes manifold height as a critical factor, significantly affecting the performance.

Fig. 12(c–d) show the effect of the ratio of inlet-to-outlet manifold width. The thermal resistance significantly reduces with decreasing the ratio (wider outlet manifold width compared to the inlet manifold). This can be attributed to the hotspot-targeted mixing enhancement from the streamwise vortex within the microchannel. Because the chips are aligned beneath the inlet manifold where a strong vortex is induced, efficient heat transfer is achieved despite the HTC being lower than the outlet manifold. This is contrary to previous studies that reported the lowest thermal resistance around $\Gamma_{io} = 3$ [22,23]. This can be attributed to the differences in the heat source condition with unit cell-based studies, where weak heat transfer below the outlet manifold becomes more pronounced when a uniform heat flux is applied across the entire base.

The pressure drop is the lowest for $\Gamma_{io} = 1$ and increases for $\Gamma_{io} < 1$ and $\Gamma_{io} > 1$ owing to the flow contraction around the inlet and outlet of the manifold.

Fig. 12(e) shows the influence of microchannel height on thermal resistance. The total thermal resistance improves with decreasing the microchannel height at 8 and 4 LPM, whereas it deteriorates at 0.5 LPM. This contrasting tendency arises because the dominance of the three factors (heat transfer area, fluid velocity, and flow uniformity) varies depending on the total flow rate. Decreasing the microchannel height provides a higher fluid velocity and improved flow distribution while decreasing the fin heat-transfer area. At a low flow rate, the fin heat-transfer area is highly effective because a low HTC allows significant heat dissipation through the microchannel wall (fin). Contrastingly, a high total flow rate has a low fin efficiency owing to its high HTC, which makes the fin heat transfer area less effective. Additionally, a high flow rate results in a more severe flow maldistribution. Therefore, the thermal resistance within 4–8 LPM was enhanced by the improved flow non-uniformity and velocity rather than the fin heat transfer area. The pressure drop changed slightly with varying microchannel heights, exhibiting a contrasting tendency. At the flow rates of 0.5 and 4 LPM, increased pressure drops with decreased microchannel height was observed owing to the decreased fluid velocity and friction loss. Contrastingly, at 8 LPM, a decreased height resulted in a slightly decreased pressure drop despite the increased friction loss within the microchannel

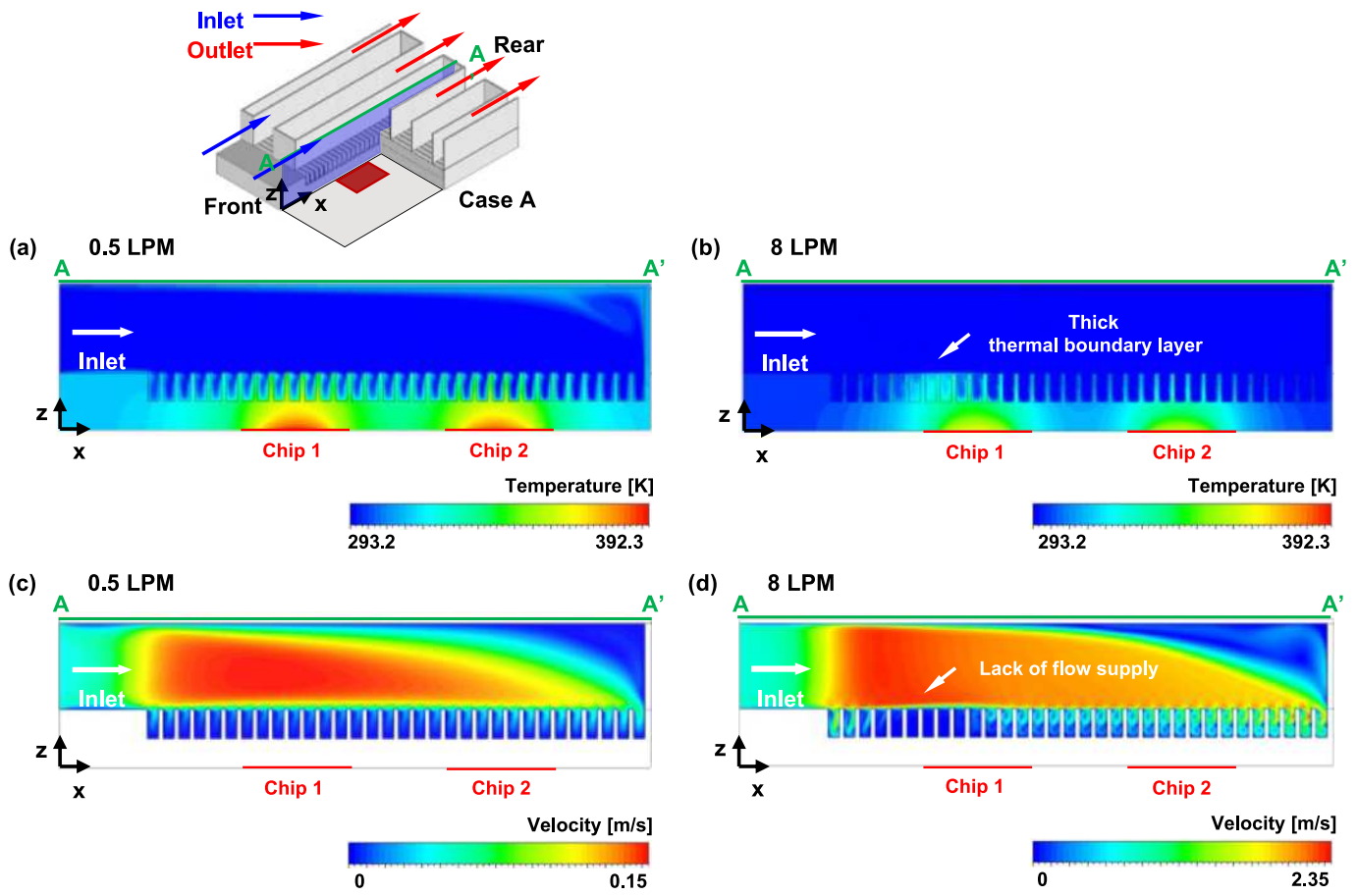


**Fig. 11. Temperature and velocity contours of the MMC heat sink at the center of the inlet manifold (Blue Plane): Temperature at (a) 0.5 LPM and (b) 8 LPM, and velocity at (c) 0.5 LPM and (d) 8 LPM.** Chip 1 (front section-cooled) exhibits a higher temperature than Chip 2 (rear section-cooled). Therefore, the lack of flow supply around the front section thickens the thermal boundary layer, thereby diminishing the convective heat transfer.

because the flow non-uniformity had a dominant impact on the pressure drop at a high flow rate. This result is contrary to previous studies that reported superior thermohydraulic performance in microchannels with aspect ratios exceeding 3. [22,24,26] This discrepancy can be attributed to the differences in the flow rate conditions, emphasizing the need for a comprehensive analysis of the geometric variable effects under the high-flow conditions that are typical of EV applications.

Fig. 13 compares the MMC heat sinks to conventional microchannel heat sinks by plotting the pumping power versus thermal resistance at (a) low and (b) high flow rates. The pumping power is defined as the product of the total flow rate and total pressure drop. The blue markers on represent the MMC designs from Cases A–J, summarizing the effect of geometrical variables at (a) 0.5 LPM and (b) 8 LPM. The optimized MMC heat sinks, marked in pink and red, employ the optimal values of the obtained geometrical variables. The height of the TMC heat sink was in the range of $H_{ch} = 1$–3 mm to comparatively evaluate the advantages of adding a manifold to it.

The MMC heat sink within the dashed outline exhibited inferior thermohydraulic performance compared to the TMC heat sinks. Employing a manifold does not always enhance thermohydraulic performance, which can be deteriorated by complex and non-uniform flow and weak convection. Appropriate geometries must be used to address these challenges. As shown in Fig. 13(a) and (b), increasing the manifold height improves the pumping power and thermal resistance by 60–70.8 % and 3.0–6.3 %, respectively. Reducing the inlet manifold width improves the thermal resistance by 3.6–8.3 % while consuming 47.9–98.4 % more pumping power. Reducing the microchannel height significantly increases the pumping power in TMC and MMC heatsinks by 233.0–317.0 % and 0.7–10.8 %, respectively. In the TMC heat sink, the pressure drop was proportional to the square of the velocity; however, this phenomenon was less apparent in the MMC heat sink owing to the reduced fluid path. Decreasing the microchannel height within the MMC heat sink improves the thermal resistance by 2.4–5.1 % and 1.2 % at 4–8 and 0.5 LPM, respectively. At low flow rates, decreasing the manifold width was the most effective in reducing the thermal resistance owing to weak convection. At high flow rates, increasing the manifold height was the most effective owing to severe flow maldistribution. In summary, to design an optimal MMC heat sink considering high total flow rates and small chips in EV power modules, the pumping power should be reduced by increasing the manifold height while enhancing the convection around the hotspot area by decreasing the inlet manifold width and microchannel height.

The thermally optimized heat sink, which is achieved by combining dimensions that present the lowest thermal resistance among the three geometric variables, is represented by pink markers ($H_m = 12$ mm, $\Gamma_{io} =$ 1:3, $H_{ch} = 3$ mm for 0.5 LPM, $H_m = 12$ mm, $\Gamma_{io} = 1{:}3$, and $H_{ch} = 1$ mm for 8 LPM). Compared with the TMC sink, two different optimal MMC geometries for 0.5 LPM and 8 LPM slightly increased the thermal resistance and substantially reduced the pumping power. By increasing the flow rate in these geometries, the optimal case, represented by the red dashed circle, helped in reducing the pumping power by 27.3 % and thermal resistance by 2.83 % at high flow rates. These reduction percentages were calculated as the difference from the TMC heat sink values and normalized. To evaluate the impact of pressure drop under high flow rate conditions, we developed a hydrodynamically optimized design using dimensions that achieve the lowest coefficient of performance

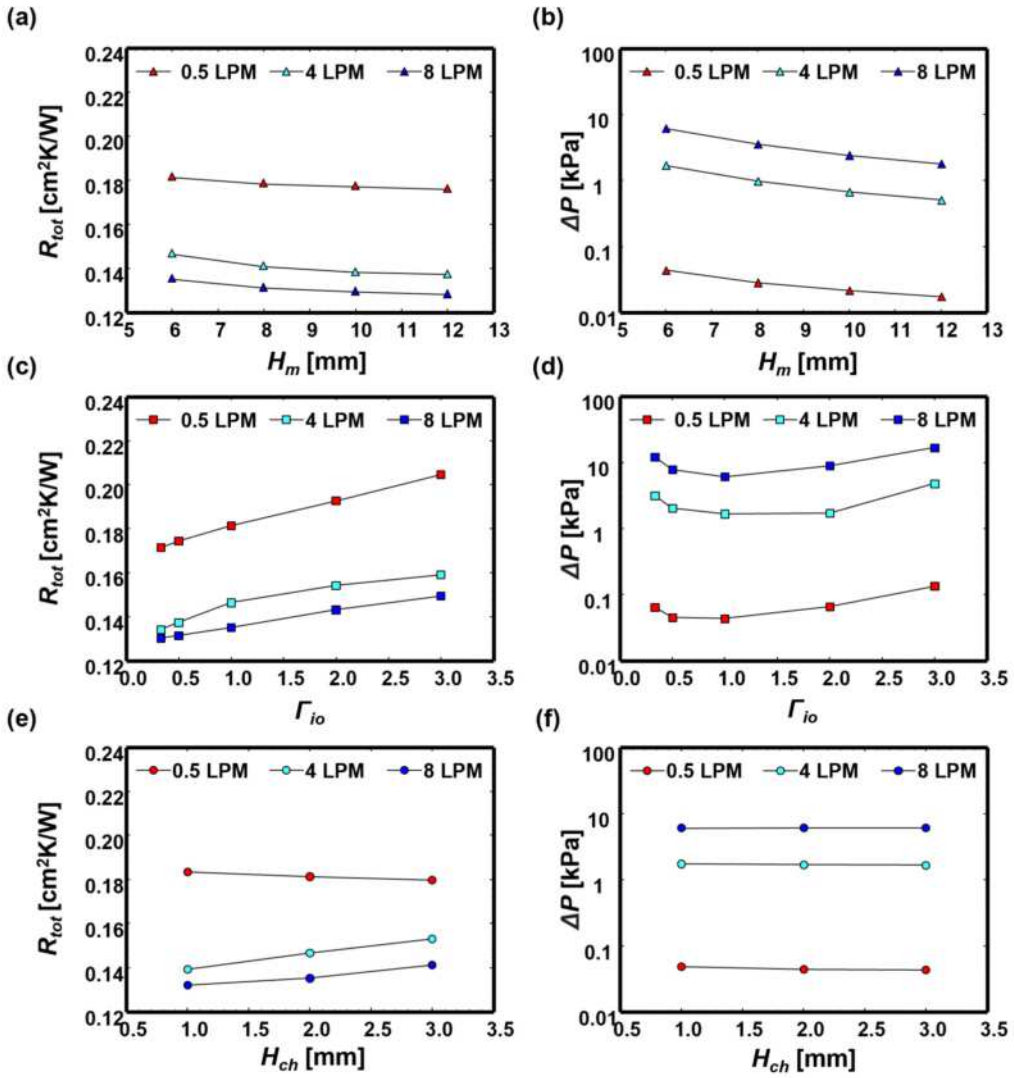


**Fig. 12. Total thermal resistance and pressure drop in various MMC heat sinks.** Variations in (a, b) manifold height, (c, d) ratio of inlet-to-outlet manifold width, and (e, f) microchannel height. Comparison at the flow rates of 0.5, 4, and 8 LPM reveals distinct trends. Independent of the total flow rate, decreased manifold width reduces thermal resistance and increased manifold height enhances pressure drop and thermal resistance. Decreased microchannel height provides a lower thermal resistance at high rate (4 and 8 LPM), whereas it results in higher thermal resistance at a low flow rate (0.5 LPM).

(COP). The COP is defined as the ratio of the heat dissipation rate at $T_{max} = 323.15$ K to the pumping power. Unlike the thermally optimized design with $\Gamma_{io} = 1{:}3$, a manifold with $\Gamma_{io} = 1{:}1$ was selected owing to its lowest pressure drop. This design exhibited inferior thermohydraulic performance when compared to the thermally optimized design, even with increased flow rates, as depicted by the red marker in Fig. 13(b). This suggests that generating focused convection at hot spots through a narrower inlet manifold is particularly effective in improving the pumping power under small heat source conditions.

Fig. 13(c) depicts the benchmarks of our designs against those reported in other studies conducted on jet impingement and TMC designs. The TMC heat sink used in this study exhibited lower thermohydraulic performance owing to the uniform convection provided across areas beyond the chip area. Conversely, the MMC design concentrated convection specifically at the chip areas, leading to slightly higher thermal resistance than jet impingement, while maintaining lower pressure losses. High-pressure forces can cause issues such as leakage or deformation, which can significantly affect the reliability of the cooling systems. Therefore, MMC cooling is a highly suitable approach for EV cooling systems.

## 4. Conclusions

A comprehensive investigation was performed to understand the impact of local heat transfer and flow distribution on the overall thermal hydraulic performance for various geometries and flow rates in an MMC heat sink. In the EV power module design characterized by a large cooler area under high flow rate conditions, distinctive flow non-uniformity and vortices within the microchannels significantly affected the overall thermohydraulic performance of the cooling systems. Based on these flow characteristics, the effects of the calculated geometrical variables are summarized as follows:

(1) Increasing the manifold height significantly enhanced the thermohydraulic performance of the MMC heat sink and improved the flow non-uniformity under high-flow-rate conditions. The pumping power and thermal resistance were reduced by 60.0–70.8 % and 3.0–6.3 %, respectively.
(2) Decreasing the inlet width led to a strong streamwise vortex within the microchannel around the hotspot area, thereby reducing the thermal resistance at low flow rates. The pumping

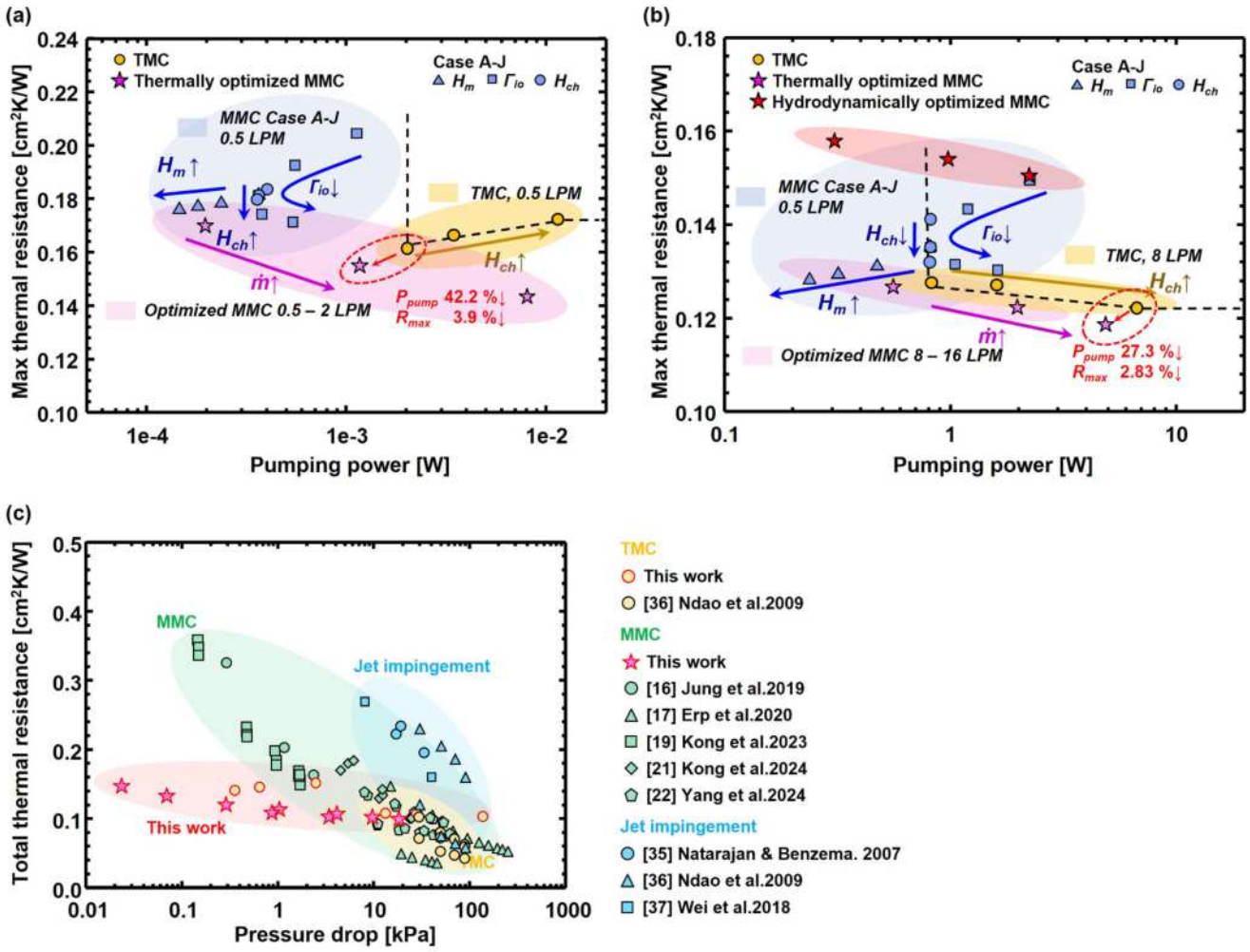


**Fig. 13. Variations in thermohydraulic performance for various MMC and microchannel heat sink designs.** (a) Low flow rates (0.5–2 LPM). (b) High flow rates (8–16 LPM), and (c) Benchmarking against other research [16,16,18,20,21,35–36].

power increased by 47.9–98.4 % when the thermal resistance reduced by 3.6–8.3 %.

(3) Variation in the microchannel height had a negligible effect on the pumping power. Decreasing the height increased the thermal resistance by 1.2 % at 0.5 and reduced it by 2.4–5.1 % at 4–8 LPM owing to the improved flow non-uniformity and streamwise vortex.

## Declaration of competing interest

The authors declare that they have no known competing financial interests or personal relationships that could have appeared to influence the work reported in this paper.

## Acknowledgments

This work was supported by the National Research Foundation of Korea (NRF) grant funded by the Korea government (MSIT) (No. RS-2024-00353227, RS-2024-00411577), and the Research Fund of the Catholic University of Korea in 2023.

## Appendix A. Supplementary data

Supplementary data to this article can be found online at https://doi.org/10.1016/j.applthermaleng.2025.125611.

## Data availability

Data will be made available on request.

## References

[1] F. Blaabjerg, H. Wang, I. Vernica, B. Liu, P. Davari, Reliability of Power Electronic Systems for EV/HEV Applications, in: Proceedings of the IEEE 109, 2021, pp. 1060–1076, https://doi.org/10.1109/JPROC.2020.3031041.

[2] F. Roccaforte, P. Fiorenza, G. Greco, R. Lo Nigro, F. Giannazzo, F. Iucolano, M. Saggio, Emerging trends in wide band gap semiconductors (SiC and GaN) technology for power devices, Microelectron. Eng. 187–188 (2018) 66–77, https://doi.org/10.1016/j.mee.2017.11.021.

[3] L. Zhang, X. Yuan, X. Wu, C. Shi, J. Zhang, Y. Zhang, Performance evaluation of high-power SiC MOSFET modules in comparison to Si IGBT modules, IEEE Trans. Power Electron. 34 (2019) 1181–1196, https://doi.org/10.1109/TPEL.2018.2834345.

[4] R. Alizadeh, T. Adamson, J.C. Balda, Y. Zhao, M. Asheghi, K.E. Goodson, A compact 50-kW traction inverter design using off-the-shelf components, in: 2019 IEEE Applied Power Electronics Conference and Exposition (APEC), 2019, pp. 2614–2619, https://doi.org/10.1109/APEC.2019.8722201.

[5] G. Zhang, H. Zou, F. Qin, Q. Xue, C. Tian, Investigation on an improved heat pump AC system with the view of return air utilization and anti-fogging for electric vehicles, Appl. Therm. Eng. 115 (2017) 726–735, https://doi.org/10.1016/j.applthermaleng.2016.12.143.

[6] Y. Ma, H. Ding, Y. Liu, J. Gao, Battery thermal management of intelligent-connected electric vehicles at low temperature based on NMPC, Energy 244 (2022) 122571, https://doi.org/10.1016/j.energy.2021.122571.

[7] L.D. Stevanovic, R.A. Beaupre, A.V. Gowda, A.G. Pautsch, S.A. Solovitz, Integral micro-channel liquid cooling for power electronics, in: 2010 Twenty-Fifth Annual IEEE Applied Power Electronics Conference and Exposition (APEC), 2010, pp. 1591–1597, https://doi.org/10.1109/APEC.2010.5433444.

[8] X. Zhang, X. Zhao, W. Li, Z. Wang, A. Liao, Y. Song, Y. Wang, L. Zhang, Ultra-thermostable embedded liquid cooling in SiC 3D packaging power modules of electric vehicles, Energ. Conver. Manage. 276 (2023) 116499, https://doi.org/10.1016/j.enconman.2022.116499.
[9] K. Gould, S.Q. Cai, C. Neft, A. Bhunia, Liquid jet impingement cooling of a silicon carbide power conversion module for vehicle applications, IEEE Trans. Power Electron. 30 (2015) 2975–2984, https://doi.org/10.1109/TPEL.2014.2331562.
[10] Y. Kim, S. Jung, S. Kim, S.T. Choi, M. Kim, H. Lee, Heat transfer performance of water-based electrospray cooling, Int. Commun. Heat Mass Transfer 118 (2020) 104861, https://doi.org/10.1016/j.icheatmasstransfer.2020.104861.
[11] N. Malu, D. Bora, S. Nakanekar, S. Tonapi, Thermal management of an IGBT module using two-phase cooling, in: Fourteenth Intersociety Conference on Thermal and Thermomechanical Phenomena in Electronic Systems (ITherm), 2014, pp. 1079–1085, https://doi.org/10.1109/ITHERM.2014.6892401.
[12] C.M. Barnes, P.E. Tuma, Practical considerations relating to immersion cooling of power electronics in traction systems, in: 2009 IEEE Vehicle Power and Propulsion Conference, 2009, pp. 614–621, https://doi.org/10.1109/VPPC.2009.5289790.
[13] N.H. Naqiuddin, L.H. Saw, M.C. Yew, F. Yusof, T.C. Ng, M.K. Yew, Overview of micro-channel design for high heat flux application, Renew. Sustain. Energy Rev. 82 (2018) 901–914, https://doi.org/10.1016/j.rser.2017.09.110.
[14] G.M. Harpole, J.E. Eninger, Micro-channel heat exchanger optimization, in: 1991 Proceedings, Seventh IEEE Semiconductor Thermal Measurement and Management Symposium, IEEE, 59–63. <https://doi.org/10.1109/STHERM.1991.152913>.
[15] K.W. Jung, C.R. Kharangate, H. Lee, J. Palko, F. Zhou, M. Asheghi, E.M. Dede, K. E. Goodson, Embedded cooling with 3D manifold for vehicle power electronics application: single-phase thermal-fluid performance, Int. J. Heat Mass Transf. 130 (2019) 1108–1119, https://doi.org/10.1016/j.ijheatmasstransfer.2018.10.108.
[16] R. van Erp, R. Soleimanzadeh, L. Nela, G. Kampitsis, E. Matioli, Co-designing electronics with microfluidics for more sustainable cooling, Nature 585 (2020) 211–216, https://doi.org/10.1038/s41586-020-2666-1.
[17] Y. Yang, J. Du, M. Li, W. Li, Q. Wang, B. Wen, C. Zhang, Y. Jin, W. Wang, Embedded microfluidic cooling with compact double H type manifold microchannels for large-area high-power chips, Int. J. Heat Mass Transf. 197 (2022) 123340, https://doi.org/10.1016/j.ijheatmasstransfer.2022.123340.
[18] D. Kong, E. Jung, Y. Kim, V.V. Manepalli, K.J. Rah, H.S. Kim, Y. Hong, H.G. Choi, D. Agonafer, H. Lee, An additively manufactured manifold-microchannel heat sink for high-heat flux cooling, Int. J. Mech. Sci. 248 (2023) 108228, https://doi.org/10.1016/j.ijmecsci.2023.108228.
[19] K. Kim, D. Kong, Y. Kim, B. Jang, J. Cho, H.-J. Kwon, H. Lee, Enhanced boiling heat transfer via microporous copper surface integration in a manifold microgap, Appl. Therm. Eng. 241 (2024) 122325, https://doi.org/10.1016/j.applthermaleng.2023.122325.
[20] D. Kong, H. Kwon, B. Jang, H.-J. Kwon, M. Asheghi, K.E. Goodson, H. Lee, Extreme heat flux cooling from functional copper inverse opal-coated manifold microchannels, Energ. Conver. Manage. 315 (2024) 118809, https://doi.org/10.1016/j.enconman.2024.118809.
[21] S. Yang, J. Li, B. Cao, Z. Wu, K. Sheng, Investigation of Z-type manifold microchannel cooling for ultra-high heat flux dissipation in power electronic devices, Int. J. Heat Mass Transf. 218 (2024) 124792, https://doi.org/10.1016/j.ijheatmasstransfer.2023.124792.
[22] J.H. Ryu, D.H. Choi, S.J. Kim, Three-dimensional numerical optimization of a manifold microchannel heat sink, Int. J. Heat Mass Transf. 46 (2003) 1553–1562, https://doi.org/10.1016/S0017-9310(02)00443-X.
[23] S. Sarangi, K.K. Bodla, S.V. Garimella, J.Y. Murthy, Manifold microchannel heat sink design using optimization under uncertainty, Int. J. Heat Mass Transf. 69 (2014) 92–105, https://doi.org/10.1016/j.ijheatmasstransfer.2013.09.067.
[24] Y.-H. Pan, R. Zhao, X.-H. Fan, Y.-L. Nian, W.-L. Cheng, Study on the effect of varying channel aspect ratio on heat transfer performance of manifold microchannel heat sink, Int. J. Heat Mass Transf. 163 (2020) 120461, https://doi.org/10.1016/j.ijheatmasstransfer.2020.120461.
[25] Y. Lin, Y. Luo, W. Li, Y. Cao, Z. Tao, T.-I.-P. Shih, Single-phase and two-phase flow and heat transfer in microchannel heat sink with various manifold arrangements, Int. J. Heat Mass Transf. 171 (2021) 121118, https://doi.org/10.1016/j.ijheatmasstransfer.2021.121118.
[26] D. Kong, Y. Kim, M. Kang, E. Song, Y. Hong, H.S. Kim, K.J. Rah, H.G. Choi, D. Agonafer, H. Lee, A holistic approach to thermohydraulic design of 3D manifold microchannel heat sinks for energy-efficient cooling, Case Stud. Therm. Eng. 28 (2021) 101583, https://doi.org/10.1016/j.csite.2021.101583.
[27] C. Chen, F. Li, X. Wang, J. Zhang, G. Xin, Improvement of flow and heat transfer performance of manifold microchannel with porous fins, Appl. Therm. Eng. 206 (2022) 118129, https://doi.org/10.1016/j.applthermaleng.2022.118129.
[28] J. Yang, K. Cheng, K. Zhang, C. Huang, X. Huai, Numerical study on thermal and hydraulic performances of a hybrid manifold microchannel with bifurcations for electronics cooling, Appl. Therm. Eng. 232 (2023) 121099, https://doi.org/10.1016/j.applthermaleng.2023.121099.
[29] S. Kumar, P.K. Singh, A novel approach to manage temperature non-uniformity in minichannel heat sink by using intentional flow maldistribution, Appl. Therm. Eng. 163 (2019) 114403, https://doi.org/10.1016/j.applthermaleng.2019.114403.S.
[30] Moreno, Thermal Performance Benchmarking: Annual Report, National Renewable Energy Lab. (NREL), Golden, CO (United States), 2016. <https://doi.org/10.2172/1247461. 684>.
[31] M. Liu, A. Coppola, M. Alvi, M. Anwar, Comprehensive review and state of development of double-sided cooled package technology for automotive power modules, IEEE Open J. Power Electron. 3 (2022) 271–289, https://doi.org/10.1109/OJPEL.2022.3166G.
[32] F.R. Menter, Influence of freestream values on k-omega turbulence model predictions, AIAA J. 30 (1992) 1657–1659, https://doi.org/10.2514/3.11115.
[33] L. Wang, J. Liu, S. Hussain, B. Sundén, Large eddy simulation of turbulent heat transfer in a non-isothermal channel: effects of temperature-dependent viscosity and thermal conductivity, Int. J. Therm. Sci. 146 (2019) 106094, https://doi.org/10.1016/j.ijthermalsci.2019.106094.
[34] G. Natarajan, R.J. Bezama, Microjet cooler with distributed returns, Heat Transfer Eng. 28 (2007) 779–787, https://doi.org/10.1080/01457630701328627.
[35] S. Ndao, Y. Peles, M.K. Jensen, Multi-objective thermal design optimization and comparative analysis of electronics cooling technologies, Int. J. Heat Mass Transf. 52 (2009) 4317–4326, https://doi.org/10.1016/j.ijheatmasstransfer.2009.03.069.
[36] T. Tiwei, H. Oprins, V. Cherman, G. Van der Plas, I. De Wolf, E. Beyne, M. Baelmans, High efficiency direct liquid jet impingement cooling of high power devices using a 3D-shaped polymer cooler, in: 2017 IEEE International Electron Devices Meeting (IEDM), 2017, pp. 32.5.1–32.5.4, https://doi.org/10.1109/IEDM.2017.8268487.